The dissipation of kinetic energy in the Lofoten Basin Eddy

Ilker Fer, Anthony Bosse, Bruno Ferron, Pascale Bouruet-Aubertot

The Dissipation of Kinetic Energy in the Lofoten Basin Eddy

ILKER FER AND ANTHONY BOSSE

Geophysical Institute, University of Bergen, and Bjerknes Centre for Climate Research, Bergen, Norway

BRUNO FERRON

University of Brest, CNRS, IFREMER, IRD, Laboratoire d'Océanographie Physique et Spatiale, IUEM, Brest, France

PASCALE BOURUET-AUBERTOT

Sorbonne Universités, UPMC, Paris, France

(Manuscript received 17 November 2017, in final form 2 March 2018)

ABSTRACT

Ocean microstructure, current, and hydrography observations from June 2016 are used to characterize the turbulence structure of the Lofoten Basin eddy (LBE), a long-lived anticyclone in the Norwegian Sea. The LBE had an azimuthal peak velocity of 0.8 m s^{-1} at 950-m depth and 22-km radial distance from its center and a core relative vorticity reaching $-0.7f$ (f is the local Coriolis parameter). When contrasted to a reference station in a relatively quiescent part of the basin, the LBE was significantly turbulent between 750 and 2000 m, exceeding the dissipation rates ε in the reference station by up to two orders of magnitude. Dissipation rates were elevated particularly in the core and at the rim below the swirl velocity maximum, reaching 10^{-8} W kg^{-1}. The sources of energy for the observed turbulence are the background shear (gradient Richardson number less than unity) and the subinertial energy trapped by the negative vorticity of the eddy. Idealized ray-tracing calculations show that the vertical and lateral changes in stratification, shear, and vorticity allow subinertial waves to be trapped within the LBE. Spectral analysis shows increased high-wavenumber clockwise-polarized shear variance in the core and rim regions, consistent with downward-propagating near-inertial waves (vertical wavelengths of order 100 m and energy levels 3 to 10 times the canonical open-ocean level). The energetic packets with a distinct downward energy propagation are typically accompanied with an increase in dissipation levels. Based on these summer observations, the time scale to drain the volume-integrated total energy of the LBE is 14 years.

1. Introduction

The Lofoten Basin of the Norwegian Sea is surrounded by the main branches of the Norwegian Atlantic Current (NwAC) carrying warm and saline Atlantic Water (AW) along the shelf break with the slope current and along the Mohn Ridge with the front current (Fig. 1) (Orvik and Niiler 2002). Between these two branches, a reservoir of deep, warm AW can clearly be identified, reaching 500–700-m depth in the climatological hydrography fields (see, e.g., Rossby et al. 2009). The region is recognized as an area of energetic mesoscale activity and of substantial heat loss to the atmosphere (Rossby et al. 2009; Richards and Straneo 2015; Raj et al. 2016; Yu et al. 2017). A long-lived, deep anticyclonic vortex is located in the central part of the basin [the Lofoten Basin eddy (LBE)] (Ivanov and Korablev 1995b,a; Søiland et al. 2016), energized by eddies shed from the slope current over the adjacent continental slope (Köhl 2007; Volkov et al. 2015; Raj et al. 2016). The LBE structure and its evolution in 3 years have been described in Yu et al. (2017) using Seaglider observations. The time evolution of the weakly stratified layers in the eddy core reveals the formation and deepening of a new core layer each winter from 2013 to 2015. The role played by the Lofoten Basin in water-mass transformation is increasingly

Denotes content that is immediately available upon publication as open access.

Corresponding author: Ilker Fer, ilker.fer@uib.no

DOI: 10.1175/JPO-D-17-0244.1

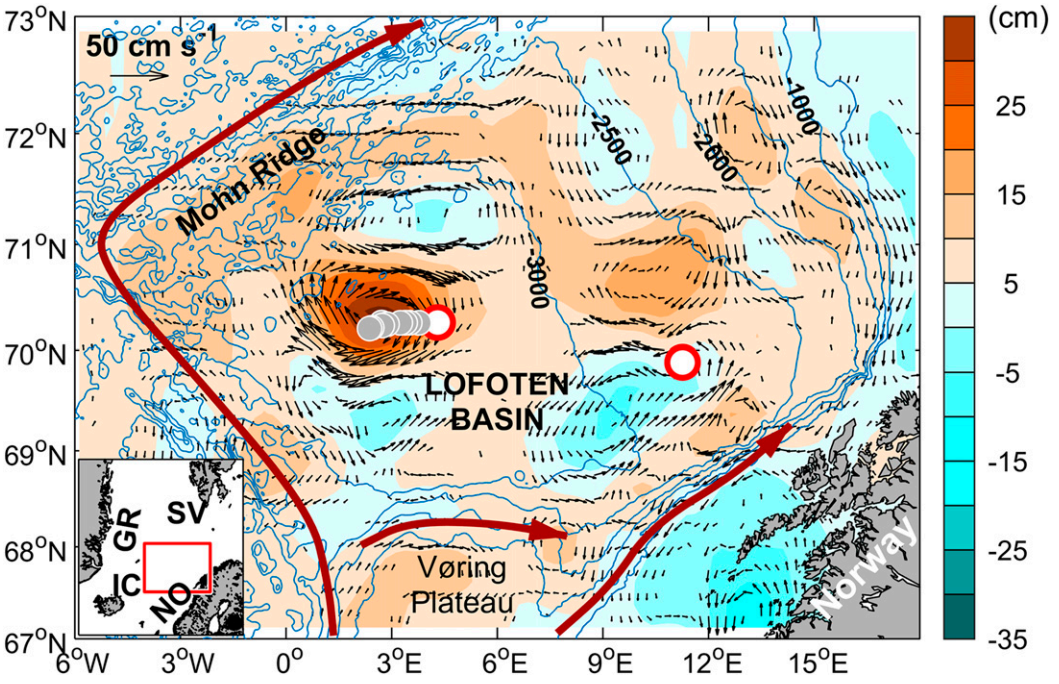

FIG. 1. Map of the study region together with the background circulation showing the main branches of the Norwegian Atlantic Current, sea level anomaly (color), and geostrophic velocity anomaly (arrows) obtained from satellite altimeter measured between 4 and 10 Jun 2016. Only values with speed greater than 5 cm s^{-1} are shown for clarity. The VMP stations near the LBE are shown with gray circles. The red outlined circles show the location of reference stations, one at 62-km radial distance from the core of the LBE (the outermost station of the section) and one at 11°E. Isobaths are drawn at 500-m intervals using the 1-arc-minute gridded global relief data ETOPO1. The inset shows the map borders (red) and Norway (NO), Svalbard (SV), Greenland (GR), and Iceland (IC).

being recognized, yet the understanding of the processes and pathways of energy transfer and mixing is incomplete. The turbulence levels and energy dissipation rates have not been studied previously in this region. Under the ''Water-mass transformation processes and vortex dynamics in the Lofoten Basin of the Norwegian Sea (ProVoLo)'' project, full-depth ocean microstructure profiles were collected in June 2016, to study the turbulent structure of the LBE in unprecedented detail.

Energy transfer associated with the vortex dynamics and vortex–vortex interactions can fuel turbulence, by increasing shear for instance; however, an additional source of energy is trapped subinertial waves. Linear internal waves can propagate freely only in the frequency range bounded by the local planetary Coriolis frequency f in the low end and the buoyancy frequency N set by vertical stratification in the high end. The negative vorticity ζ core of an axisymmetric anticyclone imposes an effective Coriolis frequency, $f_e = f + \zeta$, in a reference frame rotating with the background flow (Kunze et al. 1995; Chavanne et al. 2012), leading to $f_e < f$, hence allowing for generation and propagation of near-inertial internal waves at subinertial frequencies. Downward-propagating subinertial waves are thus trapped and amplified in the anomalous vorticity core, reflect off the eddy boundaries at horizontal turning points, and stall (zero group velocity) in critical layers (Kunze et al. 1995). The critical layer is typically at the base of the eddy and, more generally, where the minimum allowed frequency contours parallel the isopycnals (Whitt and Thomas 2013). The wave energy density amplifies as the wave approaches the critical layer, where it is trapped. Possible candidates of sink for this energy are discussed in Kunze et al. (1995), who show that bulk of the trapped energy is lost to turbulent dissipation and mixing. Microstructure observations from warm-core rings (Lueck and Osborn 1986; Kunze et al. 1995) and an anticyclone vortex cap above a seamount (Kunze and Toole 1997) show dissipation rates elevated up to two orders of magnitude at the core base, relative to the surroundings. Ray-tracing simulations reported in Kunze et al. (1995) demonstrate how near-inertial wave packets gain a considerable amount of kinetic energy to within 0.1–0.2 vertical wavelength from the critical layer in a warm core ring. In the bulk of the core, the near-inertial wave energy flux was equal within error bars to the vertically integrated turbulence production rate inferred from microstructure measurements. More recent

observations include trapped near-inertial wave packets in a warm-core ring (Joyce et al. 2013), dissipation rates elevated in a deep Southern Ocean eddy (Sheen et al. 2015), increased shear variance caused by waves trapped in submesoscale cyclonic vortex filaments in the north wall of the Gulf Stream (Whitt et al. 2018), and high dissipation rates away from the seafloor inside the midocean fracture zones, caused by transfer of near-inertial wave energy to turbulence in a critical layer (Clément and Thurnherr 2018).

Here we report on dissipation rates in the LBE, with values elevated 10–100 times above the surroundings, particularly in stratified layers with substantial background velocity shear. The source of energy to maintain the observed rates of dissipation of kinetic energy is shown to be the shear production of turbulent kinetic energy below the subsurface velocity maximum and the near-inertial energy trapped by the negative vorticity of the eddy.

2. Data

Observations were made from the Research Vessel *Håkon Mosby* during the ProVoLo summer cruise between 26 May and 15 June 2016. For a detailed description of the cruise activity, we defer to Fer (2016). Process studies were made in the LBE region as well as over the Mohn Ridge. In this study we report on a subset of the data collected near the LBE.

Figure 1 shows the sea level anomaly (SLA) and the surface geostrophic current anomaly during the LBE sampling, calculated from satellite altimeter measurements. The LBE is clearly visible as the high near 3°E, 70°N with distinct surface geostrophic velocities. The location of the eddy seen on satellite data agrees with the cruise observations. As we will show in section 3, the stations cover the core and periphery of the LBE and extend outside the eddy; however, the surface geostrophic currents inferred from satellite measurements have a much larger footprint. The coarse effective resolution is a result of gridding and optimal interpolation methods applied to the along-track SLA data to produce the gridded dataset (see, e.g., Raj et al. 2016). Yu et al. (2017) reported that the LBE radii inferred from satellite were approximately a factor of 2 larger than those obtained from Seaglider observations. Also note the energetic basin with currents associated with cyclones and anticyclones. Detailed location of the stations and the position of the eddy core are shown in Fig. 2 together with the upper-ocean current vectors measured from the vessel.

a. Temperature and salinity measurements

Conductivity–temperature–depth (CTD) profiles were acquired using a Sea-Bird Scientific, SBE 911plus system, with pressure, temperature, and salinity data accurate to ±0.5 dbar, $\pm 2 \times 10^{-3}$ °C, and $\pm 3 \times 10^{-3}$, respectively. Of a total of 46 CTD profiles, 15 were in the LBE region. The CTD data were processed using the SBE software following the recommended procedures. A total of 45 salinity samples were analyzed, and no correction was necessary (the RMS difference between the bottle- and CTD-derived salinity before and after correction were $\pm 3.5 \times 10^{-3}$ and $\pm 3.3 \times 10^{-3}$, respectively, comparable to the measurement accuracy). Conservative Temperature Θ, Absolute Salinity S_A, and potential density anomaly referenced to surface pressure σ_θ are calculated using the thermodynamic equation of seawater (McDougall et al. 2010).

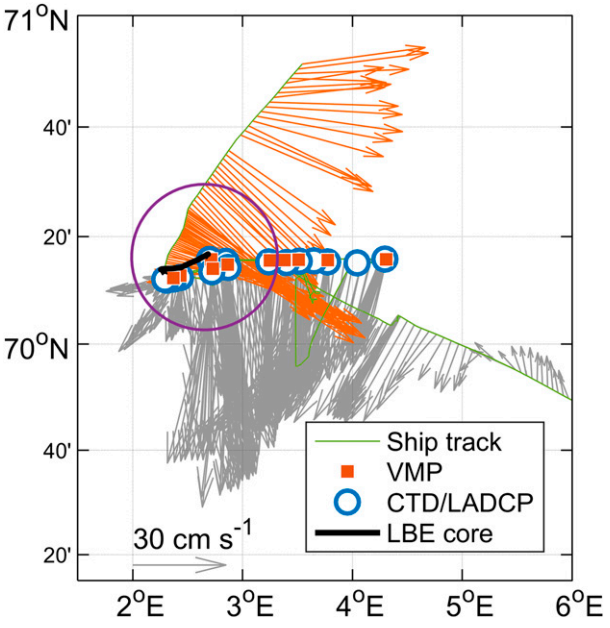

FIG. 2. Detailed view of the sampling near the LBE. Vectors show the currents sampled by the VMADCP, vertically averaged between 100 and 500 m, for the period between 2000 UTC 3 Jun 2016 and 0000 UTC 8 Jun 2016. Thick black curve shows the changing location of the LBE core, estimated using the current measurements. An arbitrary 25-km-range ring is shown for reference (i.e., it does not outline the LBE), centered at the time of first core location. Gray vectors are collected when progressing inward to the LBE and working stations, whereas the orange vectors are when the ship steamed out of the LBE uninterrupted.

b. Current measurements

Current profile measurements were made using acoustic Doppler current profilers (ADCPs). The CTD rosette was fitted with two 300-kHz Teledyne RD Instruments Workhorse lowered ADCPs (LADCPs), collecting 1-s profiles in master–slave mode in 8-m vertical bins. The LADCP was set to sample in 39 (including all 15 profiles collected in the LBE region) out of

46 CTD casts, giving simultaneous stratification and horizontal current profiles at each CTD/LADCP station. The LADCP data were processed using the velocity inversion method of Visbeck (2002), implemented in the LDEO software version IX-12, with typical horizontal velocity uncertainty of 2–3 cm s^{-1} (Thurnherr 2010). The *Håkon Mosby* was equipped with a 75-kHz Teledyne RD Instruments ocean surveyor vessel-mounted ADCP (VMADCP), which sampled approximately every 1.5 s, in 16-m vertical bins throughout the cruise. The VMADCP data were processed using the University of Hawaii software, to 2-min averages (i.e., 80 pings). Using the manufacturer's single ping accuracy, the 2-min averaged currents were accurate to ± 0.014 m s^{-1}. Typical final processed horizontal velocity uncertainty is 2–3 cm s^{-1}. All current measurements are corrected for the magnetic declination.

c. *Microstructure measurements*

Ocean microstructure measurements were made using untethered, free-fall vertical microstructure profilers (VMPs) VMP5500 and VMP6000 and a tethered VMP2000 with a line-puller winch system. All VMPs are manufactured by Rockland Scientific International (RSI), Canada. During the cruise, 61 microstructure profiles were collected in total, in the Lofoten Basin and in the Mohn Ridge region. Of these, 29 were collected using the telemetered VMP2000 system, and 32 using the internal recording deep VMPs. During the LBE survey, the VMP2000 was not appropriately grounded, resulting in noisy shear probe data in all 12 LBE casts, which are excluded from the study of the LBE. In this paper, we present dissipation measurements only from the free-fall VMPs (four profiles from VMP5500 and seven from VMP6000). Typically, the VMP was deployed 10–15 min before a CTD/LADCP profile, giving collocated, approximately simultaneous measurements of stratification, currents, and microstructure. The two deep VMPs were used sequentially to increase the profiling frequency and to allow sufficient time to charge the internal main battery. The fall rate of the instrument was 0.6 m s^{-1} near the surface and linearly decreased to 0.5 m s^{-1} at 3000 dbar. Each VMP was equipped with SBE temperature (SBE3F) and conductivity (SBE4C) sensors, a pair of FP07 thermistors, and a pair of shear probes. The shear probes were installed with their axis of sensitivity orthogonal to each other. We did not experience systematic or random deviations between the shear channels on any of the VMPs. The noise level for the dissipation rate of turbulent kinetic energy per unit mass ε was lower than 10^{-11} W kg^{-1}.

The processing of the microstructure data is based on the routines provided by RSI (ODAS v4.01) (Douglas and Lueck, 2015), and the dissipation rate calculations follow the RSI Technical Notes 028 and 039 (https://rocklandscientific.com/support/knowledge-base/technical-notes/; R. Lueck 2017, personal communication), using 2-s FFT length and half-overlapping 8-s segments for dissipation calculations. We opted for the RSI routines with an aim toward reproducibility and standardization; independent processing using the routines of the French team (e.g., Ferron et al. 2014) and the Norwegian team (e.g., Fer et al. 2014) gave similar profiles. Additionally, we corrected the sensitivity of the shear probes for the in situ water temperature (a sensitivity loss of approximately 1% per °C relative to the calibration temperature of about 20°C). Dissipation rates were quality screened, inspecting the individual spectra as well as the instrument accelerometer records and cross-checking between the two shear probes. Good-quality measurements were then averaged over the two estimates, except when the two measurements differed by more than a factor of 10, the minimum dissipation value was used.

3. Radial section across the eddy

A radial section across the LBE is obtained after referencing the stations to the eddy center. The location of the eddy center is detected in 36-h intervals using the 0–500-m depth-average currents from the VMADCP, following Bosse et al. (2015). Their method is devised for ocean glider data; however, it is applicable to depth-averaged currents from VMADCP, as similarly done by Nencioli et al. (2008). All profiles of horizontal velocity are then projected onto azimuthal v and radial u components (right-handed coordinate system).

Once all the stations are referenced to the eddy center, the radial section is constructed using all available profiles of currents and hydrography, using optimal interpolation with Gaussian correlation length scales of 20 km in horizontal and 100 m in vertical. These scales are representative of the eddy radius and the thickness of the deep pycnocline driving the balanced flow of the eddy. For the horizontal velocity, all LADCP profiles and 1-km horizontally bin-averaged VMADCP profiles are pooled together for optimal interpolation. The vertical component of vorticity is calculated as $\zeta = 1/r\partial(rv)/\partial r$, where r is the radial distance from eddy center.

The radial distribution of LBE (Fig. 3) shows the doubly convex structure of density surfaces within approximately 30 km from the detected center of the core, where relatively colder and less saline waters (relative to the outer radial distances where isopycnals flatten) are found in the surface layer and warm and saline water in the deeper part of the vortex. The 27.8 kg m^{-3}

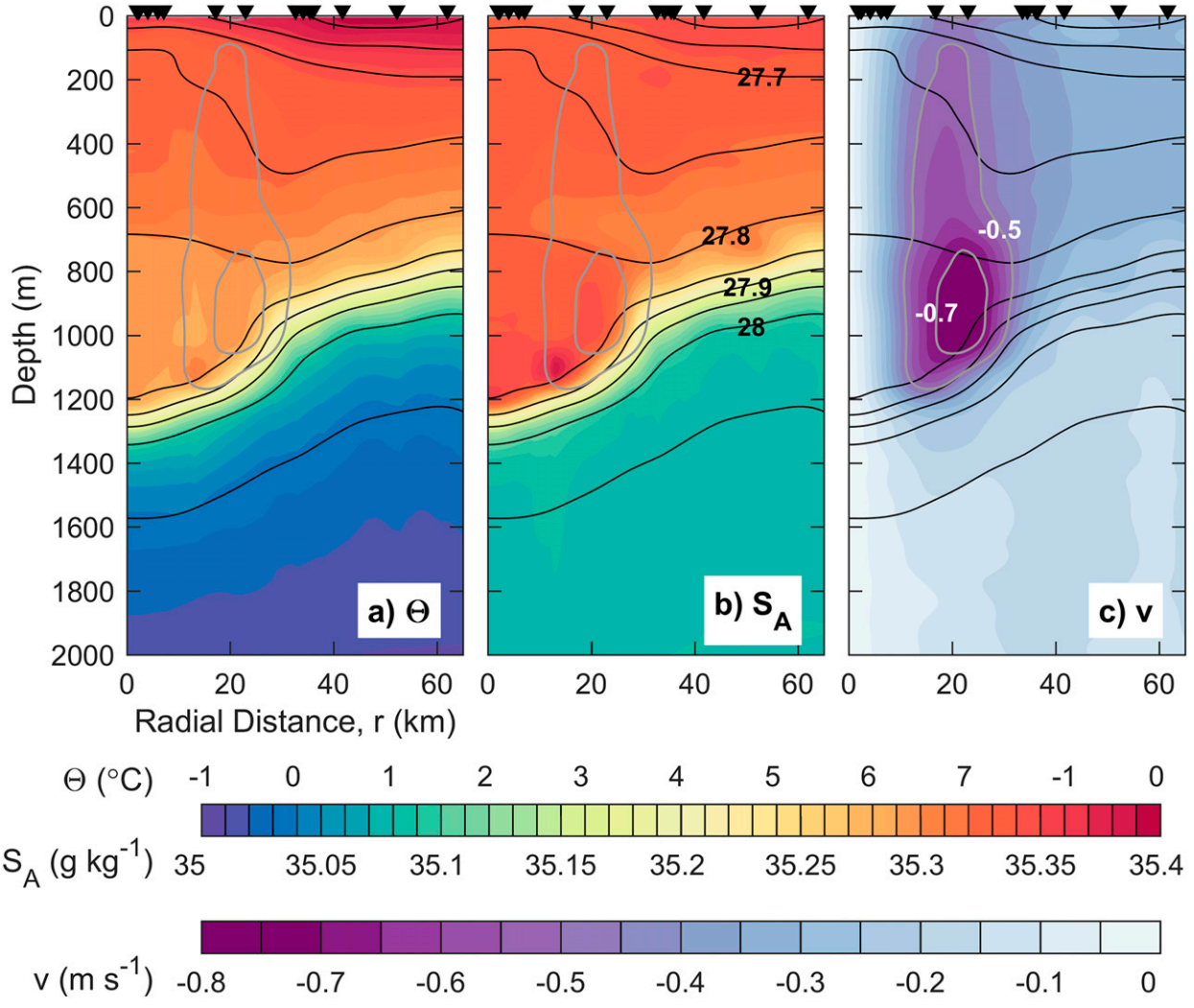

FIG. 3. Radial sections of (a) Conservative Temperature Θ, (b) Absolute Salinity S_A, and (c) azimuthal velocity, v, obtained from the CTD/LADCP profiles collected at positions indicated at the top. In each panel, v contours for -0.5 and $-0.7\,\mathrm{m\,s^{-1}}$ are marked for reference. Black contours are for the potential density anomaly σ_θ at $0.05\,\mathrm{kg\,m^{-3}}$ intervals. Sections are obtained by referencing each station to a time-variable core position (at $r = 0$) and using optimal interpolation with correlation length scales of 20 km (horizontal) and 100 m (vertical).

isopycnal separates two well-mixed layers of approximately 400-m thickness. The base of the vortex is characterized by the pycnocline at 1300-m depth in the core separating warm and saline AW from the deep waters below, shoaling to 800 m at the outer edge of the eddy. A subsurface azimuthal velocity maximum of approximately $0.8\,\mathrm{m\,s^{-1}}$ is found at 950-m depth, $r = 22$ km (Fig. 3c). The core of LBE has large negative vorticity, typically $-0.5f$ and larger (Fig. 4a), reaching $-0.7f$ at 6 km and 840 m. These can be compared to the recent Seaglider observations reported in Yu et al. (2017). Averaged over eight realizations of the LBE sampled between July 2012 and July 2015, the mean radius was 18 km with a peak azimuthal velocity of 0.5–$0.7\,\mathrm{m\,s^{-1}}$ located at depths between 700 and 900 m, with the minimum vorticity of $-0.7f$ to $-0.9f$ near the eddy axis. This is also in agreement with earlier shipborne ADCP measurements showing extreme negative vorticity (close to $-f$) near the LBE axis (Søiland et al. 2016).

The radius of deformation calculated from the phase speed of the first baroclinic mode, $R_1 = c_1/f$, is 12 km, where c_1 is obtained from numerical solution of the Sturm–Liouville form, using the reference buoyancy frequency profile at 60-km radial distance. This classical definition of the internal deformation radius is typically larger than the deformation radius R_d of a localized anomalous volume of water trapped in submesoscale coherent vortices. For the LBE, with a typical density anomaly of $0.1\,\mathrm{kg\,m^{-3}}$, $R_d = \sqrt{g\rho'/\rho_r}h/f$, is 8 km using a thickness of $h = 1200$ m. The density anomaly ρ' is

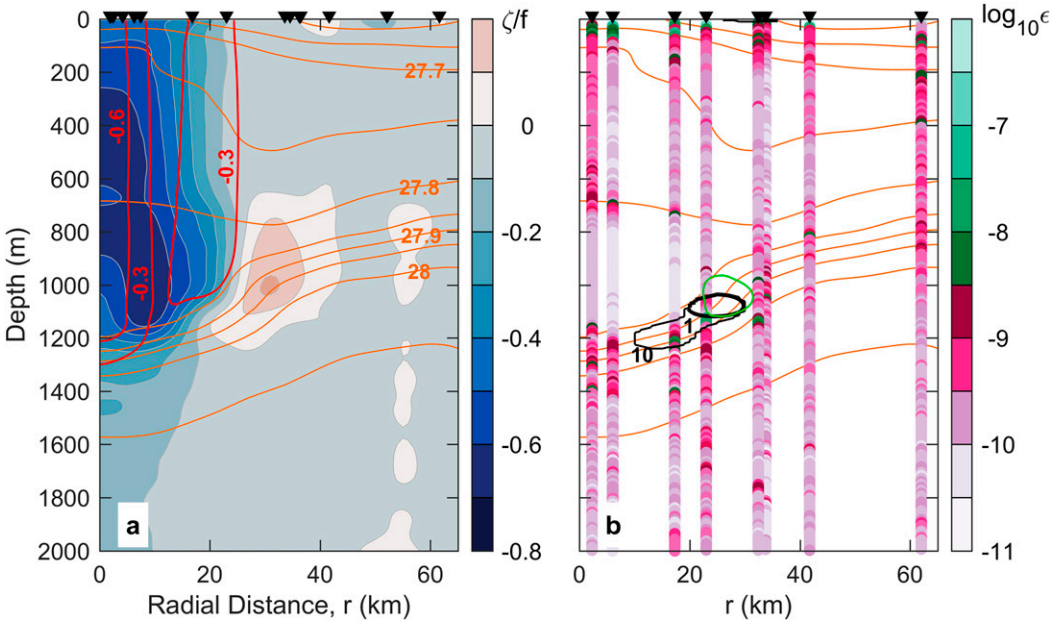

FIG. 4. Radial sections of (a) Rossby number $\mathrm{Ro} = \zeta/f$ and (b) dissipation rate ε ($\log_{10}$; W kg^{-1}). Vorticity ζ is derived from the optimally interpolated field of v collected at stations marked at the top. Additionally the Rossby number of the balanced flow, $\mathrm{Ro}_0 = \zeta_0/f$, is shown with red contours. Orange contours in both panels are for σ_θ at 0.05 kg m^{-3} intervals. Profiles of ε measured by the deep VMPs at the marked positions are 10-m vertically averaged. Additionally in (b) the background Ri, using S^2 and N^2 from the gridded fields of observations, is contoured in black for Ri = 1 (thick) and Ri = 10 (thin). The green contour is for $\mathrm{Ri}_0 = 10$ where Ri_0 is the Richardson number of the balanced flow, obtained from the thermal wind shear.

calculated as the vertically averaged value of the differences between profiles at 60 km and in the core, ρ is the potential density, and ρ_r is the reference density.

Combining the horizontal force balance (Coriolis, pressure gradient, and centrifugal forces) with hydrostatic balance for a baroclinic circular vortex gives the gradient wind balance:

$$\left(f + \frac{2v_0}{r}\right)\frac{\partial v_0}{\partial z} = \frac{\partial b_0}{\partial r}, \tag{1}$$

where variables associated with the balanced vortex are indicated by the subscript 0, v is the azimuthal velocity, r is the radial distance from the center of the vortex, and $b = -g\rho/\rho_r$ is the buoyancy [see also appendix B of Joyce et al. (2013)]. Note that the right-hand side of Eq. (1) is related to the geostrophic vertical shear, $M^2 = \partial b_0/\partial r = f\partial v_g/\partial z$, where v_g is the geostrophic velocity.

We calculate the balanced azimuthal flow by solving Eq. (1) for v_0, after calculating the geostrophic shear from the optimally interpolated, smooth background density field. The geostrophic vertical shear is made absolute using the observed (smoothed) velocity field at 1800-m depth, chosen to ensure a level sufficiently below the subsurface velocity maximum. The maximum of the balanced flow is similar to the total v, 0.75 m s^{-1}, but located at 26-km and 800-m depth. The Rossby number of the balanced flow, $\mathrm{Ro}_0 = \zeta_0/f$, is lower than -0.6 near the core (Fig. 4).

4. Dissipation rates in the LBE

Profiles of dissipation rates overlain on the radial section of isopycnals show that elevated ε is typically concentrated near the density surface separating the two pycnostads and in the main deep pycnocline located at the base of the LBE (Fig. 4b). The turbulent segments near $r = 20$ km below the velocity maximum are characterized by small background gradient Richardson number Ri between 1 and 10. Ri does not resolve the small scales associated with turbulent mixing and is calculated from the objectively interpolated fields of velocity and stratification, as $\mathrm{Ri} = N^2/S^2$, where $S^2 = (\partial u/\partial z)^2 + (\partial v/\partial z)^2$. Ri estimates can be corrupted by segments of weak shear and stratification where the vertical gradients are close to the instruments' noise levels. We exclude values when N^2 and S^2 are less than 10^{-6} s^{-2}, approximately corresponding to a noise level in vertical gradients of velocity and density of 1 cm s^{-1} and 10^{-3} kg m^{-3} over a 10-m vertical scale, respectively.

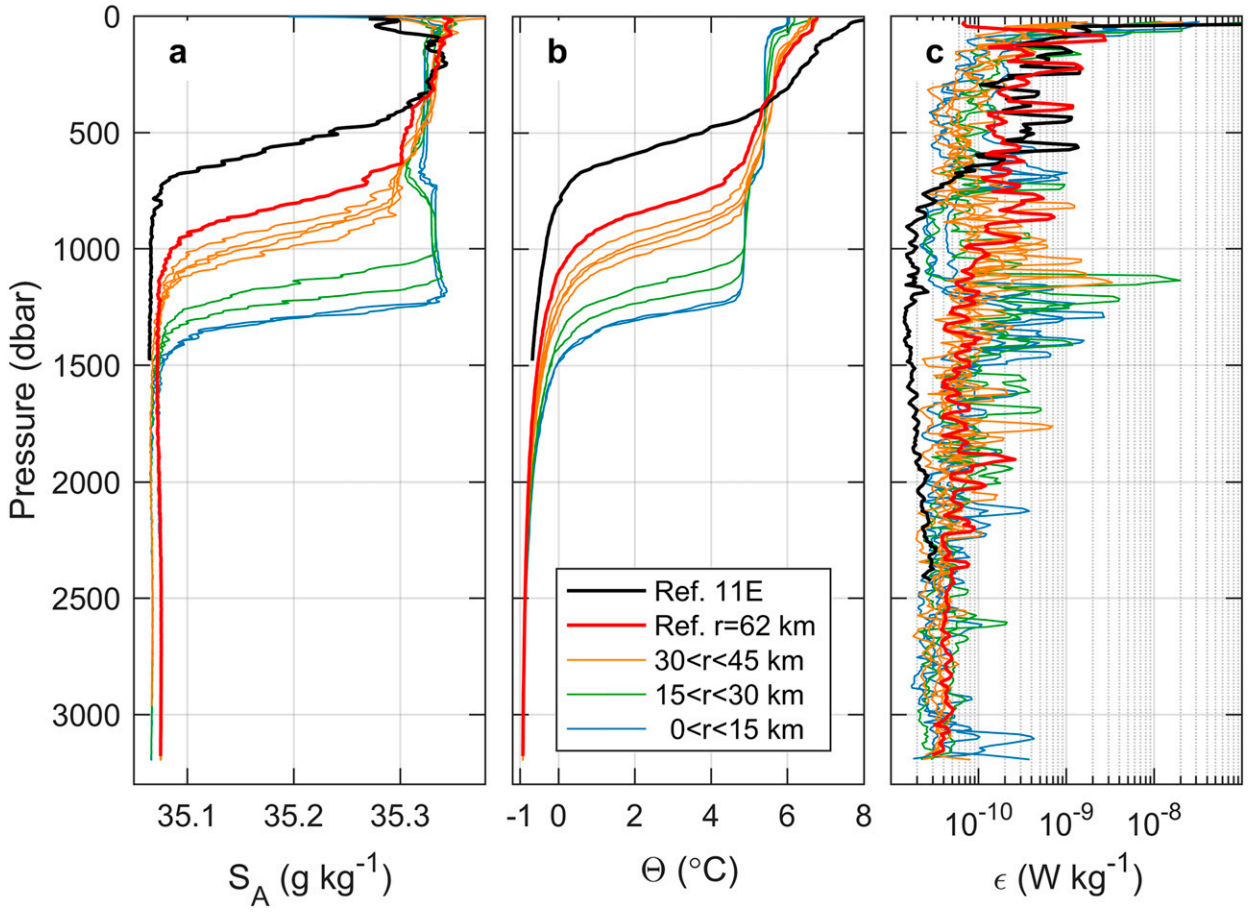

FIG. 5. Vertical profiles of (a) S_A, (b) Θ, and (c) ε from two reference stations (marked in Fig. 1) and from the LBE stations at indicated radial distance ranges from the core center ($r = 0$). All profiles are from the sensors on the VMPs. Salinity and temperature are vertically smoothed over 10 m and dissipation profiles are smoothed over 30 m.

Note that the vertical resolution of the ADCP measurements, vertical averaging, and smoothing involved in optimal interpolation result in Ri calculated over the averaging scales typically larger than mixing events. Even the Ri_0 calculated using the balanced flow reaches values as low as 10 (red contour in Fig. 4b). While well-resolved values of Ri less than 1/4 imply shear-generated turbulence, values of Ri calculated here up to Ri = 10 could be suggestive of mixing events.

Individual profiles of dissipation rate within the LBE show elevated subsurface turbulence levels between 750- and 2000-m depth (Fig. 5). When contrasted to a reference station farther east in the basin (black line in Fig. 5), dissipation rates in the LBE are up to two orders of magnitude larger. This energetic structure is particularly strong in the core and at a radial distance near the velocity maximum at two levels concentrated near the pycnoclines, with a quiescent segment between them. Another reference station is the outermost station of the section, at 62-km radial distance from the core (red line in Fig. 5). At this outer station, the dissipation rates in the upper part of the water column are comparable to the eastern part of the basin, but there is elevated turbulence at the pycnocline, and the background turbulence level is higher than the eastern reference station. Relatively high levels of turbulence outside the LBE imply dynamic interactions and transfer of energy between the eddy and the ambient. Compared to this station, the inner part of the LBE is more turbulent in the 1000–1500-m depth range. At the outer part of the LBE, profiles collected between 30 and 45 km from the center have a different vertical structure with a single energetic layer centered at the main deep pycnocline. Note that the large dissipation values in the bottom 100 m of profiles near the core are approximately 200 m above the seabed and cannot be directly associated with bottom friction.

Dissipation profiles from core stations and stations near the velocity maximum are replotted in Fig. 6,

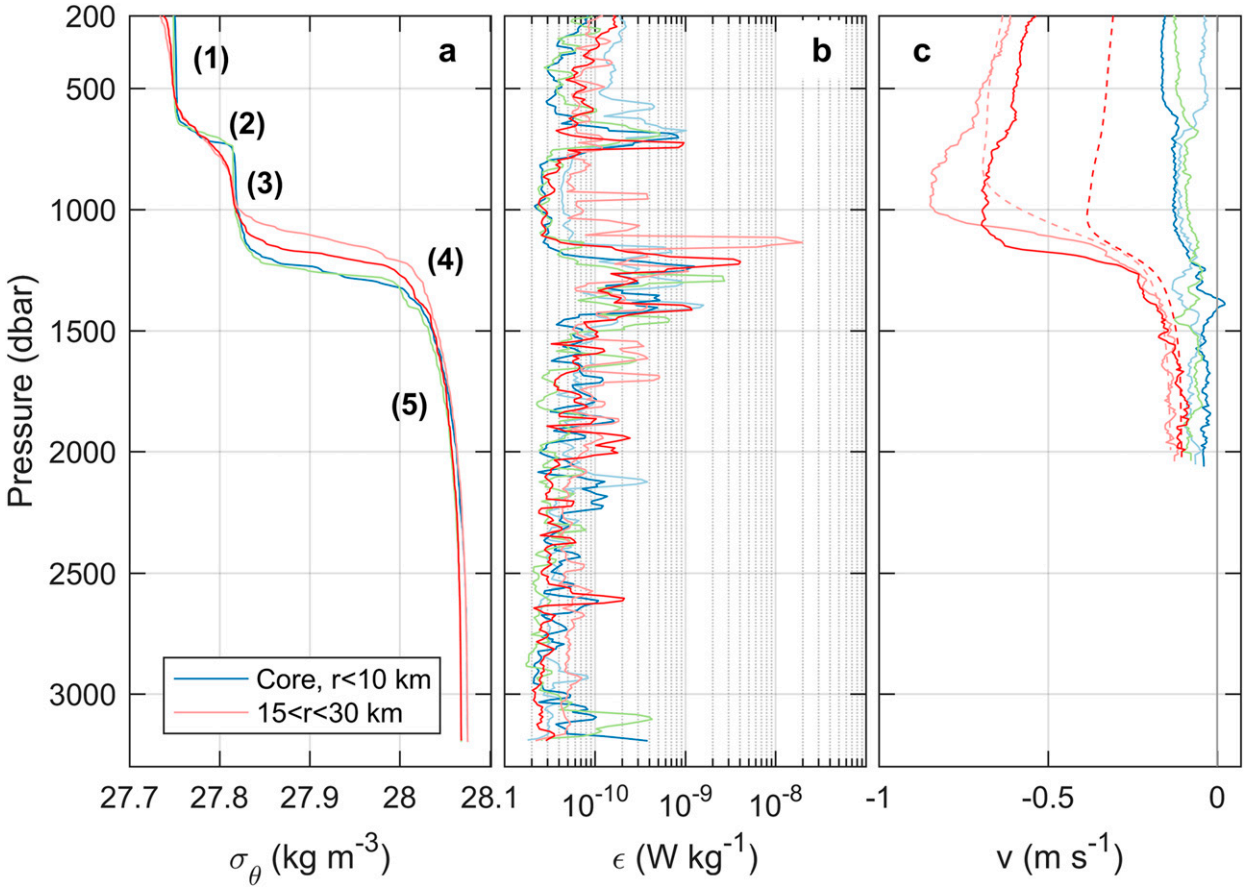

FIG. 6. Vertical profiles of (a) σ_θ, (b) ε, and (c) v for the stations in the core (r within 10 km, two stations with warm colors) and near the velocity maximum (three stations with cold colors). Also shown are the balanced flow profiles near the velocity maximum (dashed curves). In (a), representative layers identified when discussing the vertical structure are indicated: upper pycnostad (1), upper pycnocline (2), deeper pycnostad (3), deeper pycnocline (4), and base of the LBE (5). Density and dissipation rate profiles are from the sensors on VMPs, smoothed over 10 and 30 m, respectively. The velocity profiles are obtained from the LADCP system, down to 2000 m, deployed shortly after the corresponding VMP casts.

together with density and velocity profiles, to highlight the collocation of pycnoclines, strong subsurface shear, and dissipative layers. For ease of reference, in Fig. 6a we identify five layers in the vertical density profile: upper pycnocstad, upper pycnocline, deeper pycnostad, deeper pycnocline, and base of the LBE. There is a clear correspondence of strong shear and high dissipation rates near the velocity maximum, in the deeper pycnocline (layer 4). The increase in turbulence levels in the upper pycnocline (layer 2), however, is not associated with the shear from the eddy swirl.

The possibility of shear production of TKE in layers associated with low Ri, particularly below the velocity maximum, is further supported by computing higher-resolution and better-resolved (compared to the objectively analyzed fields) Ri using profiles of stratification, finescale shear, and dissipation rate from collocated CTD/LADCP and VMP cast pairs. All profiles of velocity, density, and ε are vertically averaged to 8 m (the scale of LADCP processing) to be consistent, and the vertical gradients (for shear and stratification) are obtained over 32-m vertical scale to exclude the high-wavenumber noise in LADCP shear. The gradients are computed from the slope of a line fit of density or velocity components against depth, over five moving data points. Again, noisy data are further eliminated by excluding segments with N^2 and S^2 less than 10^{-6} s^{-2}. We would expect the segments with low Ri to be associated with dissipation rates elevated above the background levels. The low Ri here is primarily caused by an increased shear as a result of the high shear zone beneath the subsurface velocity maximum or the focusing and amplification of the trapped near-inertial shear near critical layers (section 6). Because of the variability in location and length scale of the turbulence generating processes and the limited set of measurements, the 32-m Ri is not expected to show an abrupt transition (a critical value)

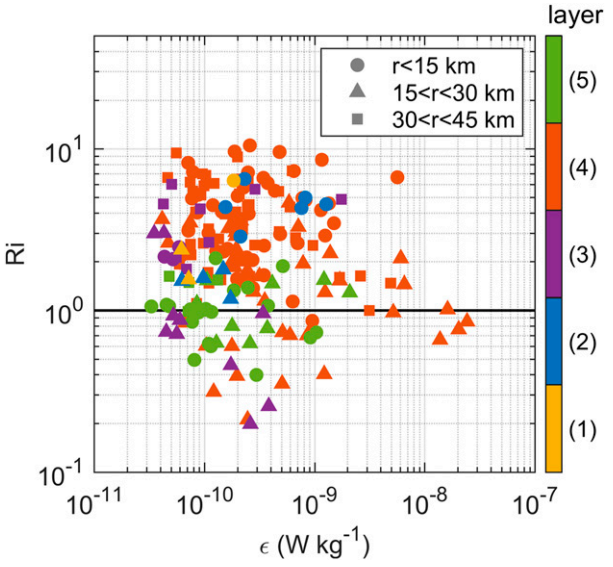

FIG. 7. Scatter diagram of Ri vs ε calculated from collocated CTD/LADCP–VMP cast pairs. Different markers for radial distance are used, color coded for vertical layers indicated in Fig. 6a. The layers are defined by isopycnals: 1) upper pycnostad ($27.75 < \sigma_\theta \leq 27.78\,\mathrm{kg\,m^{-3}}$), 2) upper pycnocline ($27.78 < \sigma_\theta \leq 27.81\,\mathrm{kg\,m^{-3}}$), 3) deeper pycnostad ($27.81 < \sigma_\theta \leq 27.85\,\mathrm{kg\,m^{-3}}$), 4) deeper pycnocline ($27.85 < \sigma_\theta \leq 28.02\,\mathrm{kg\,m^{-3}}$), and 5) the base of the LBE ($28.02 < \sigma_\theta \leq 28.06\,\mathrm{kg\,m^{-3}}$). Horizontal line marks Ri = 1. All profiles are vertically averaged to 8 m (bin size of LADCP processing), and the vertical gradients for shear and stratification are obtained over 32 m (five data points).

from background levels to turbulent levels with increased ε. Nevertheless, a large number of segments in the core and near the velocity maximum has Ri less than unity (Fig. 7). The largest dissipation values occur near the velocity maximum at the rim (deeper pycnocline, layer 4, $15 < r < 30$ km in Fig. 7). Dissipation rates near the base of the core are also elevated above the background level ($r < 15$ km, layer 5 in Fig. 7), where Ri is equal to or less than unity.

5. Energetics

Available potential energy (APE) of the LBE is computed following the method outlined in Hebert (1988) assuming an axisymmetric eddy and a reference station averaged between 60 and 65 km from the eddy center and integrating over the eddy volume, radially and vertically. For the APE calculations potential density referenced to 1000 dbar is used, which is appropriate for the depth range of the LBE. Horizontal kinetic energy (HKE; $\mathrm{HKE} = \int 0.5\rho_r(u^2 + v^2)\,dV$) is computed over the same volume V, using both the azimuthal and radial components of the velocity. Calculations of APE and HKE with volumes for increasing radial distance out to 60 km show that APE reaches a plateau at approximately $r = 35$ km. HKE continuously increases with r (u and v do not asymptotically approach zero at the periphery of the eddy). For the analysis of LBE, we choose $r = 35$ km for the radial extent and 100- to 1400-m depth for the vertical extent of integration (note that isopycnals do not level even down to 1800 m depth). Extending the vertical integration from surface to 1600 m increases APE and HKE by 8% and 7%, respectively.

The energy Burger number, Bu_E = HKE/APE, averaged (±one standard deviation) over 5 km centered at 35 km is 1.75 ± 0.01, with HKE = 5.9×10^{14} J and APE = 3.4×10^{14} J. For reference, HKE computed from the balanced v_0 is approximately equal to the total HKE. Using VMADCP surveys from 2010 to 2015, Søiland et al. (2016) report total HKE and total potential energy for the LBE, using velocity measurements only, integrated over the uppermost 500 m and out to 60 km. Their values vary between 1×10^{14} and 5×10^{14} J for total HKE and between 1×10^{15} and 5×10^{15} J for total potential energy, yielding Bu_E on the order of 0.1 (i.e., 10–20 times less than our observations). The difference in the integration volume could be one reason for the discrepancy, but repeating our calculation for a volume integral in the upper 500 m and out to 60 km, similar to Søiland et al. (2016), yields similar HKE whereas APE decreases by one order of magnitude, thereby increasing the disagreement with Søiland et al. (2016). The upper 500 m excludes the deep swirl velocity maximum layer, and extending the volume to 60 km incorporates more of the kinetic energy from the surroundings into the eddy, which may somewhat compensate. The total potential energy inferred from velocity measurements in Søiland et al. (2016) likely contains a large amount of potential energy, which is not necessarily quantified as APE, leading to the disagreement in Bu_E.

The dissipation rate profiles are gridded (linear interpolation) onto the same radial section to infer the volume integrated dissipation of TKE. The average value of ε in the same radial (0–35 km) and vertical (100–1400 m) extent of the eddy is $4 \times 10^{-10}\,\mathrm{W\,kg^{-1}}$, yielding a volume-integrated total dissipation of $\varepsilon_I = \rho_r \int \varepsilon\,dV = 2 \times 10^6$ W. An alternative calculation using the objectively interpolated field of dissipation rate, and carrying out the integration identical to HKE and APE calculations gives similar results. The time scale for eddy decay, (HKE + APE)/ε_I, is then estimated to be approximately 14 years. It takes 9 years to drain the balanced HKE alone. The deep currents in the core are strong, suggesting barotropic currents of order $0.1\,\mathrm{m\,s^{-1}}$ (Fig. 3). A 200-m-thick bottom boundary layer with an average dissipation rate of $5 \times 10^{-10}\,\mathrm{W\,kg^{-1}}$ would drain the kinetic energy of a

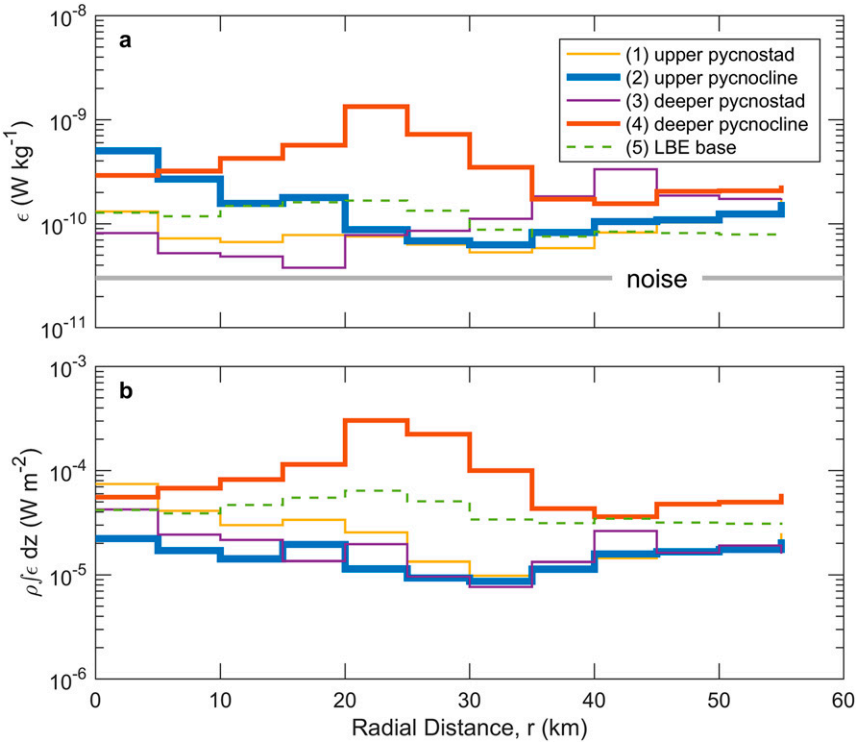

FIG. 8. Dissipation rates as a function of radial distance, vertically (a) averaged and (b) integrated between isopycnals outlining the upper pycnostad, upper pycnocline, deeper pycnostad, deeper pycnocline, and base of the LBE. For reference, the approximate depth of the isopycnals bounding the layers, averaged within $r < 10$ km, are 120, 650, 720, 1180, 1380, and 1700 m (see also Fig. 6a). The noise level of the VMP profiler is indicated in (a).

20-km radius, 3300-m-thick water column in approximately 21 years.

Layer-averaged and layer-integrated dissipation rates are the largest in the deeper pycnocline (layer 4; $27.85 < \sigma_\theta \leq 28.02\,\mathrm{kg\,m^{-3}}$), particularly over the radial distance from 15 to 35 km, covering the velocity maximum (Fig. 8). While the dissipation averaged over the upper pycnocline is the largest in the core region ($4 \times 10^{-10}\,\mathrm{W\,kg^{-1}}$), its contribution to the total dissipation is relatively small because of the limited volume. In terms of volume-integrated dissipation in the eddy center ($r < 5$ km), the base of the eddy, the deeper pycnocline, and the upper pycnostad contribute equally. Throughout the radial section, the deep layer (5; LBE base) and the deeper pycnocline (layer 4) are the main sinks for energy. The deep layer contributes largely because of the expansive volume, whereas the deeper pycnocline has much smaller volume but large dissipation rates, particularly near the velocity maximum. This region is also where Ri values are the smallest (close to unity inferred from background fields, in Fig. 4b; less than unity inferred from individual casts, in Fig. 7).

6. Amplification of energy by trapped near-inertial waves

The minimum frequency of inertia–gravity waves allowed within a baroclinic axisymmetric vortex was derived by Joyce et al. (2013, appendix B), based on Whitt and Thomas (2013), as

$$\omega_{\min} = (f_e^2 - f^2 \mathrm{Ri}_0^{-1})^{1/2}, \tag{2}$$

where f_e is the effective Coriolis frequency given by

$$f_e = [(f + 2v_0/r)(f + \zeta_0)]^{1/2}, \tag{3}$$

and the Richardson number of the balanced flow is $\mathrm{Ri}_0 = N^2/(\partial v_g/\partial z)^2 \equiv f^2 N^2/M^4$.

The depth–radius changes in stratification, shear and vorticity in the LBE allow subinertial waves with low frequencies. Three examples of $\omega_{\min}$ contours ($0.8f$, $0.9f$, and $0.95f$) are shown in Fig. 9. The lowest frequency is limited to the core of the eddy and the velocity maximum region, limited to the base of the eddy, whereas the higher frequencies are allowed throughout the water column. Slab-mixed layer calculations of near-inertial

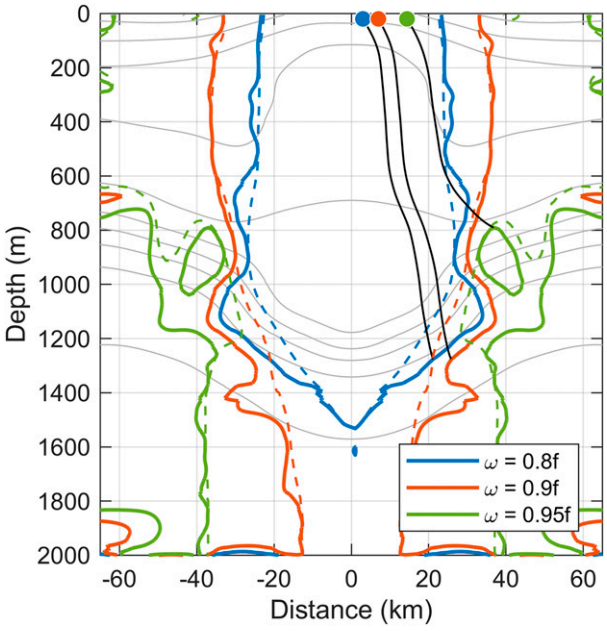

FIG. 9. Contours of effective inertial frequency (dashed) and minimum allowed frequency ω_{min} (solid) for near-inertial wave packets with 0.8*f*, 0.9*f*, and 0.95*f* in the LBE. Isopycnals at 0.05 kg m^{-3} intervals are shown for reference (gray lines). Note that only one-half of the eddy is sampled, which is mirrored for presentation. Three selected characteristics are shown in black (one for each frequency indicated by corresponding marker colors at the release depth of 50 m) and are used for the calculations of Fig. 13.

oscillations in a unidirectional, laterally sheared geostrophic current forced by oscillatory wind stress show that the resonance forcing frequency is the effective Coriolis frequency (Whitt and Thomas 2015). Throughout stormy periods, any of these example frequencies are plausible to resonate in the eddy. The analogy with Whitt and Thomas (2015) can be taken further: if we assume constant wind direction over the typical eddy rotation period of 1–2 days, an oscillatory wind stress can be achieved as a result of the eddy rotation. For the peak azimuthal velocity of $v = 0.8\,\mathrm{m\,s^{-1}}$ at $r = 20$ km, the rotation frequency v/r is approximately 0.3*f*. We have not examined further the possible energy amplification from such very low subinertial frequencies, but calculations similar to those presented in Fig. 9 show patchy ω_{min} contours in the core region, in the upper and deeper pycnostads (not shown).

Ray paths (characteristics) and properties (e.g., group velocity, wavenumber) of wave packets with selected subinertial frequencies are calculated using the formulation from Whitt and Thomas (2013), using the algorithm applied to the north wall of the Gulf Stream in Whitt et al. (2018). The MATLAB code used for the calculation of Fig. 10 of Whitt et al. (2018) was kindly provided by Dan Whitt (and is available at https://github.com/danielwhitt/WhittThomas2013raytracing; https://doi.org/10.5281/zenodo.1183395). The caveats of applying the ray-tracing theory are discussed in detail in Whitt and Thomas (2013) and Whitt et al. (2018). We also note that the extension of the ray-tracing and numerical solution applied here is not strictly valid in curved flows, and the results from this analysis should be viewed with caution. Examples of internal wave characteristics with ω equal to 0.8*f* and 0.95*f* are shown in Fig. 10. The waves are released every 5-km at 50-m depth and traced to illustrate the turning points and critical layers. The traces of rays depend on where in the water column they originate and are only presented to highlight how the background vorticity, shear, and stratification reflect and focus the beams of near-inertial energy. The characteristics with $\omega = 0.8f$ focus at the base of the eddy whereas those with higher frequency do not. The evolution of the group velocity and energy of the rays depends on the initialized wave vector. Vertical wavenumber spectra from the observations and profiles of amplitude and phase of the baroclinic HKE are used as guidelines to infer wave vector parameters for more detailed ray-tracing calculations below.

Vector spectral analysis of velocity or shear profiles are often used to identify the vertical propagation of near-inertial waves (e.g., Fer et al. 2010). Wind-generated near-inertial waves are typically clockwise (CW) polarized, and the dominance of CW variance indicates upward phase and downward energy propagation (Leaman and Sanford 1975). For flows with $O(1)$ Rossby and Richardson numbers, propagating wave packets on steep characteristics can, however, be in opposite direction (Whitt and Thomas 2013). CW and counterclockwise (CCW) rotary vertical wavenumber spectra are calculated using the individual LADCP profiles (projected on to radial and azimuthal components). The azimuthal and radial velocity anomalies (baroclinic velocity; v' and u') are calculated by removing the background balanced flow interpolated from the gridded field to the station position. Half-overlapping 1024 m long segments (FFT length of 128 points) below 200-m depth are analyzed and spectra are averaged in the core region, near the velocity maximum and at the outer edge of the eddy (Fig. 11). To obtain the shear spectra, velocity spectra are multiplied by $(2\pi k_z)^2$, where k_z is the cyclic vertical wavenumber. Each segment is linearly detrended to remove a low-frequency remnant after removing the balanced counterpart (see Fig. 6 for a comparison of v and v_0). The spectra are noisy because only 12, 6, and 10 spectra are averaged, from the core to the outer edge, respectively. We truncate the spectra at vertical scales less than 30 m and do not apply corrections to account for the attenuation at

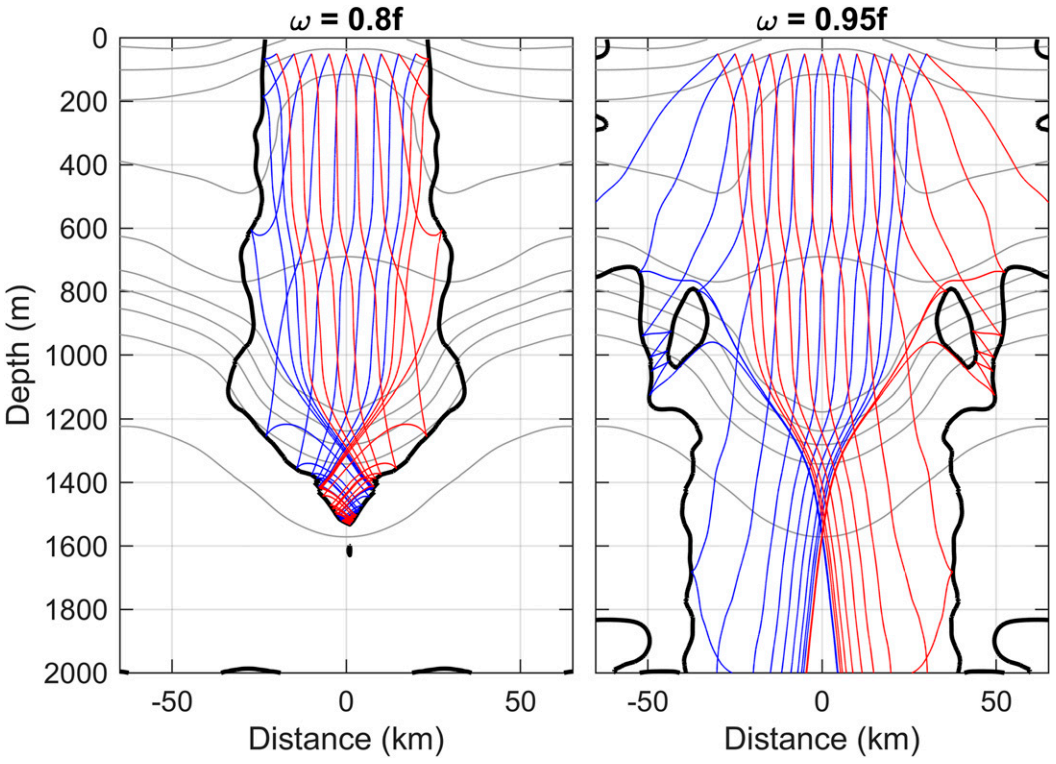

FIG. 10. Trajectories (characteristics) of near-inertial internal waves with frequencies (left) $\omega = 0.8f$ and (right) $\omega = 0.95f$. Waves are released at 50-m depth every 5 km (opposing directions in blue and red, respectively). Gray contours show the background density field at 0.05 kg m^{-3} intervals and the thick black contour is the minimum allowed frequency $\omega_{\min}$. The perfect symmetry of the background field is because the sampled half of the eddy is mirrored.

high wavenumbers as a result of sampling, processing, and averaging effects (Polzin et al. 2002).

Several inferences can be made from these spectra. In contrast to the outer radial distances, the energy in the core and rim is elevated above the Garrett and Munk (GM) level (Garrett and Munk 1975; Cairns and Williams 1976). The GM level is typical of open-ocean interior, and the spectra suggest that the LBE region is energized. There is an energetic high-wavenumber peak in the CW component, corresponding to approximately 70-m vertical scale, with 3 to 10 times the GM level. Shear variance outside the eddy is small, with no distinct polarization. Altogether, the spectra suggest an amplification of high-wavenumber CW energy, typically associated with downward-propagating near-inertial waves.

The vertical wavelengths of the energetic near-inertial wave packets are estimated following Kunze et al. (1995). The observed baroclinic horizontal velocity phase is computed as $\phi = \arctan(v', u')$. For energetic wavepackets, with ϕ uniformly changing with depth, the vertical wavelength λ_z can be estimated from the slope of line fit of ϕ against z. Decreasing ϕ with depth indicates upward phase and downward energy propagation (Leaman and Sanford 1975). The baroclinic horizontal kinetic energy density is calculated as $\mathrm{HKE_{bc}} = 0.5(u'^2 + v'^2)$. An energetic wave packet is defined as that having $\mathrm{HKE_{bc}}$ above 3×10^{-3} J kg^{-1}, the GM level representative of the typical ocean background internal wave energy. Examples of wave packets detected for cast 477, at $r = 1.8$ km, and cast 490, at $r = 2.4$ km, are shown in Fig. 12, and properties from 14 detected events are tabulated in Table 1. Vertical wavelengths range from 100 m to the LBE core extent. The $\mathrm{HKE_{bc}}$ is typically 2 to 5 times the GM level. The energetic packets are also accompanied with increases in dissipation levels (Fig. 12). The lack of clear phase propagation and the large vertical wavelengths (i.e., larger than 73 m found in spectra) can be attributed to the difficulty in detecting the trapped near-inertial waves that have their energy amplified in a very limited vertical extent. This can be exemplified by detailed wave properties along three selected characteristics (Fig. 13).

Vertical group velocity, vertical wavelength, and $\mathrm{HKE_{bc}}$ along a ray can be calculated for an initialized wave vector by solving the ray-tracing equations

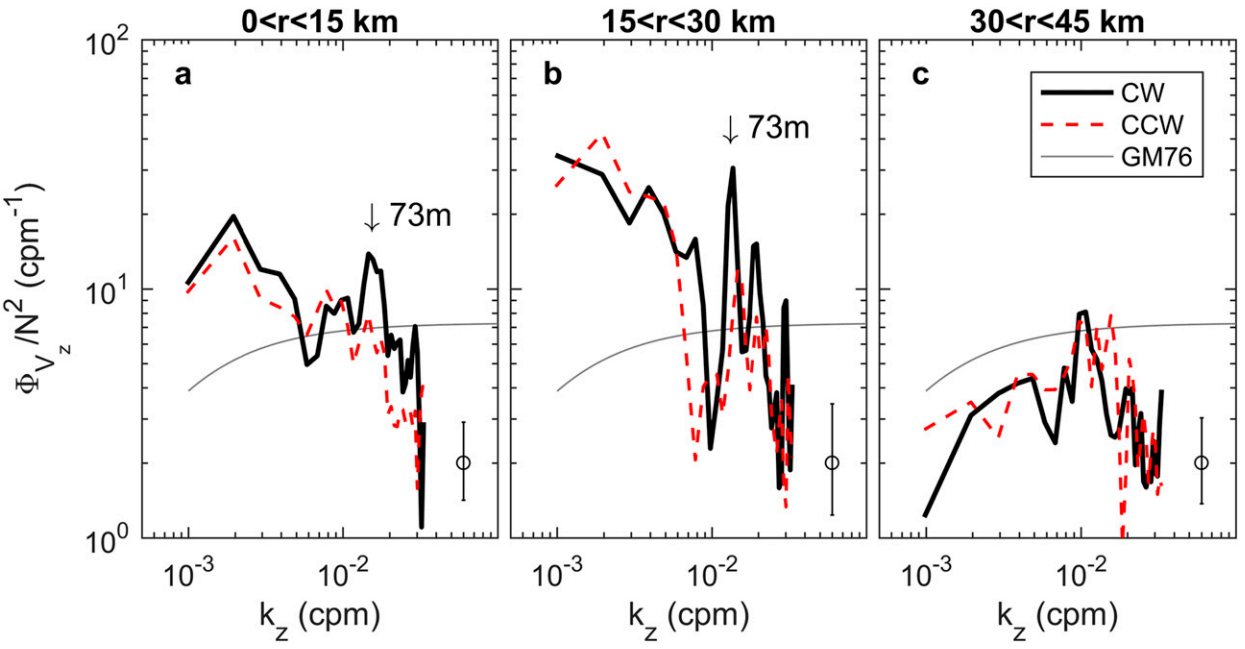

FIG. 11. Vertical wavenumber spectra of shear, normalized by buoyancy frequency, for CW (black) and CCW (dashed red) rotary components, averaged from all LADCP profiles between radial distance (a) 0–15 km, core region (12 spectra); (b) 15–30 km, rim region (6 spectra); and (c) 30–45 km, outside the eddy (10 spectra). Spectra are calculated using the baroclinic velocities, after removing the balanced component, and over 128 data points between 200–2000 m (vertical sampling of 8 m corresponds to approximately 1-km segment length). The 95% confidence intervals and the Garrett and Munk (Garrett and Munk 1975; Cairns and Williams 1976) spectrum are also shown. Spectra are truncated at 30-m vertical scale to remove the high-wavenumber noise. The wavenumber with energetic CW variance in the core and rim region is marked by an arrow and corresponds to a vertical wavelength of 73 m.

(Whitt et al. 2018). Note, however, that in these solutions the effects of curvature are being neglected. While the structure of vertical wavenumber and frequency can be assumed continuous, because of the limited lateral extent of a vortex, the radial structure does not form a continuum but will be quantized in modes in radial and azimuthal wavenumbers (Kunze and Boss 1998). We do not have information on the horizontal wavenumber of the near-inertial waves in the LBE (attempts to extract information on the horizontal wavenumber using the VMADCP data were not successful). Based on the typical eddy diameter of approximately 50 km, we choose a wavelength of 100 km and check sensitivity for 50 and 150 km. Guided by the observations, we choose a wave vector with a terminal vertical wavelength between 70 and 100 m and with $\mathrm{HKE_{bc}} = 10^{-2}\,\mathrm{J\,kg^{-1}}$ (i.e., we seek these properties when the wave approaches a turning point or a critical layer and then trace the rays backward in time). Because of the rapid decay of vertical wavelength and energy near the critical layer, the results are not sensitive to these choices (Fig. 13). Three examples are traced with frequencies of 0.8*f*, 0.9*f*, and 0.95*f*. The position of the ray trajectories in the eddy radial section can be seen in Fig. 9 (thin lines).

The profiles of time elapsed to reach the terminal depth (inferred from integration of vertical group velocity), vertical wavelength, and $\mathrm{HKE_{bc}}$ show that the wave energy propagation is very slow close to the critical layer, and the wave uses several days to cover less than 50 m vertically, during which period its wavelength reduces from over 1000 m to 100 m and its energy is amplified from near zero to $10^{-2}\,\mathrm{J\,kg^{-1}}$. These profiles are similar to those reported in Kunze et al. (1995). Clearly, it is very difficult to detect distinct wave packets in individual LADCP profiles in energetic layers of such short vertical extent, and both the energy levels and wavelengths of the packets, summarized in Table 1, are plausible.

7. Diapycnal mixing and *N* dependency

Diapycnal mixing in the Lofoten Basin was previously mapped (Naveira Garabato et al. 2004), as a part of a broader Nordic Seas survey, using finescale parameterizations based on the internal wave energy content relative to the GM level (Polzin et al. 1995). The parameterization accounts for the non-GM conditions and high near-inertial energy via a dependence on the shear-to-strain ratio. The CTD/LADCP

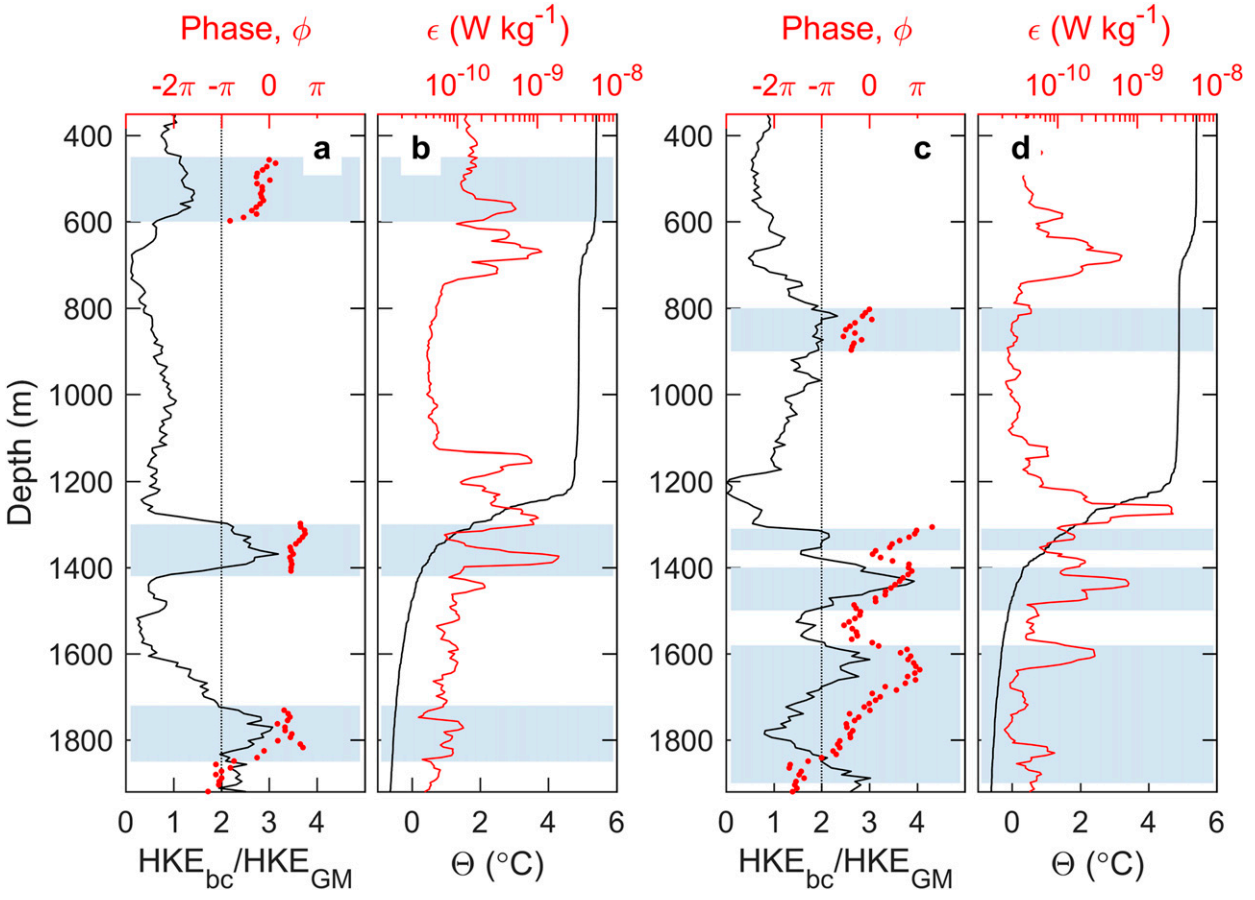

FIG. 12. Example of near-inertial wave packets observed (left) on 1307 UTC 4 Jun 2016 (CTD/LADCP profile 477) and (right) on 0739 UTC 7 Jun 2016 (CTD/LADCP profile 490). Also shown are the dissipation profiles from VMP, taken approximately 1 and 5 h, respectively, before the CTD/LADCP profiles. (a),(c) Vertical profile of baroclinic HKE normalized by the GM level (30×10^{-4} J kg^{-1}) and relative phase ϕ (red dots, shown only for energetic events for clarity). The vertical dotted line is the normalized HKE equal to 2, for reference. The shading marks depth ranges where several packets with elevated energy and upward phase (downward energy) propagation were detected. (b),(d) Profiles of Θ and ε. Dissipation profile is 5-m vertically averaged and further smoothed using three-point moving average for presentation.

profiles from the Lofoten Basin showed particularly weak diapycnal diffusivity (K is of order 10^{-5} m^2 s^{-1}) in the upper and intermediate layers of the central Lofoten Basin. The basin-averaged profile showed a relative minimum in both ε and K at approximately 1500 m, separating the distinct regimes dominated by surface energy sources and downward energy propagation from top layers and deep energy sources and upward energy propagation from bottom layers, respectively. From these measurements, the vertically integrated rate of turbulent kinetic energy in the central Lofoten Basin was in the range of 2–3 $\times$ 10^{-3} W m^{-2} (with an uncertainty of a factor of 3). In comparison, full-depth integrated dissipation rate from our averaged profile is 2 $\times$ 10^{-3} W m^{-2}, in support of the finescale parameterization inferred value reported in Naveira Garabato et al. (2004). Overall, this is 4 times the LBE depth-integrated value (100–1400 m, 0–35 km) of 5 $\times$ 10^{-4} W m^{-2}.

Using all 10 microstructure profiles in the LBE (i.e., excluding the reference station at 11°E), we construct survey-averaged profiles (Fig. 14) by vertically averaging in 50-dbar bins (isobaric) and in 0.02 kg m^{-3} σ_θ bins (isopycnic). Below a near-surface turbulent layer driven by forcing at the surface, the averaged dissipation profile shows a quiescent water column with increased turbulence near 700 and 1200 m, corresponding to the signature of turbulence in layers 2 and 4. Averaging in pressure bins smears out the vertical structure of dissipation, because of the varying levels of turbulence in strongly tilted isopycnals in cyclogeostrophic balance. Isopycnally averaged profiles are more representative of the turbulence structure in the LBE. Diapycnal diffusivity is estimated as $K = 0.2\varepsilon N^{-2}$

TABLE 1. Properties of the observed energetic wave packets with upward phase propagation. Cast is the CTD/LADCP profile cast number, r is the radial distance from the LBE center, z_s and z_e are the start and end depths of the packet, $\mathrm{HKE_{bc}/HKE_{GM}}$ is the measured horizontal kinetic energy of the package scaled by the GM level, k_z is the vertical wavenumber, k_{err} is the percent error, and λ_z is the vertical wavelength.

Cast	r (km)	z_s–z_e (m)	$\mathrm{HKE_{bc}/HKE_{GM}}$	k_z (rad m^{-1})	k_{err} (%)	λ_z (m)
477	1.8	450–600	1.3	0.011	22	571
477	1.8	1300–1420	2.4	0.015	22	419
477	1.8	1720–1850	2.5	0.019	33	331
486	23.0	790–970	4.2	0.047	9	134
486	23.0	1600–1850	1.6	0.042	3	150
487	16.8	1400–1820	4.7	0.035	2	180
488	6.2	1550–1650	1.9	0.032	15	196
489	4.1	1380–1790	2.6	0.025	2	251
490	2.4	800–900	2.0	0.012	37	524
490	2.4	1310–1360	2.0	0.051	10	123
490	2.4	1400–1500	2.9	0.039	8	161
490	2.4	1580–1900	1.9	0.026	5	242
491	2.0	1370–1420	2.2	0.029	29	217
491	2.0	1630–1700	1.7	0.041	12	153

(Osborn 1980), using the common value of 0.2 (related to the efficiency of diapycnal mixing). Care should be taken when including the weakly stratified segments in the calculations, and we report values using all data segments and using only averages over segments with N^2 above the noise level of $10^{-6}\,\mathrm{s}^{-2}$ (see section 4). Bouffard and Boegman (2013) show that the Osborn relation is valid for the intermediate values of turbulence intensity $\varepsilon/(\nu N^2)$ between 8.5 and 400, where ν is the molecular viscosity (taken as $2 \times 10^{-6}\,\mathrm{m^2\,s^{-1}}$ here). For more energetic turbulence, the mixing efficiency decreases with increasing turbulence intensity, resulting in overestimated K values when the Osborn model is used. In our dataset, turbulent intensity below 100 m or below the $\sigma_\theta = 27.7\,\mathrm{kg\,m^{-3}}$ surface, is always between 10 and 300, independent of the choice of averaging; hence the estimates of K using the Osborn model can be considered accurate.

When averaged isopycnally, the dissipation profile follows a similar shape as N^2 (Fig. 14), implying $\varepsilon \sim N^2$ as suggested by Polzin et al. (1995). A power-law fit as $\varepsilon \sim N^a$, using all 24 isopycnally averaged data points, results in $a = 1.8 \pm 0.4$. Below the $27.7\,\mathrm{kg\,m^{-3}}$ isopycnal and throughout the eddy, the diapycnal diffusivity shows a very narrow range of variability whereas N^2 varies by over two orders of magnitude. This suggests that finescale parameterizations, after accounting for the non-GM conditions through the shear-to-strain ratio, can be skillful in predicting the dissipation profile here.

8. Summary

We presented the first observations of dissipation rates in the long-lived anticyclonic vortex located in the deepest part of the Lofoten Basin, often referred to as the Lofoten Basin eddy (LBE). Observations are limited to one snapshot during a summer cruise in June 2016 but cover the full water depth for microstructure and the upper 2000 m for stratification and currents. The transect across the eddy is used to present the structure of stratification, currents, and turbulent dissipation of the LBE and to quantify its dynamical features and volume-integrated energy. We discuss the sources of energy that can drive the observed turbulence and present observational evidence that supports contributions from the subinertial energy trapped by the negative vorticity of the eddy and from the production of turbulent kinetic energy by background shear below a subsurface swirl velocity maximum.

In June 2016, the LBE can be characterized by a subsurface azimuthal velocity maximum of approximately $0.8\,\mathrm{m\,s^{-1}}$ at 950-m depth located at 22-km radial distance from the eddy center and a core with large negative vorticity reaching $-0.7f$. Our observations of hydrography and currents complement the earlier observational studies that used satellite altimetry data, lacked concurrent sampling of hydrography and currents (e.g., ocean gliders sampled only hydrography and inferred current profiles from depth-averaged currents; shipborne current profiler surveys lacked hydrographic measurements), or were limited in vertical extent (gliders to 1000 m, current profilers to 500–700 m), thereby not sufficiently resolving the deep velocity maximum and the full-depth structure of the eddy. The dynamical features of the LBE reported here are typically in agreement with earlier observations.

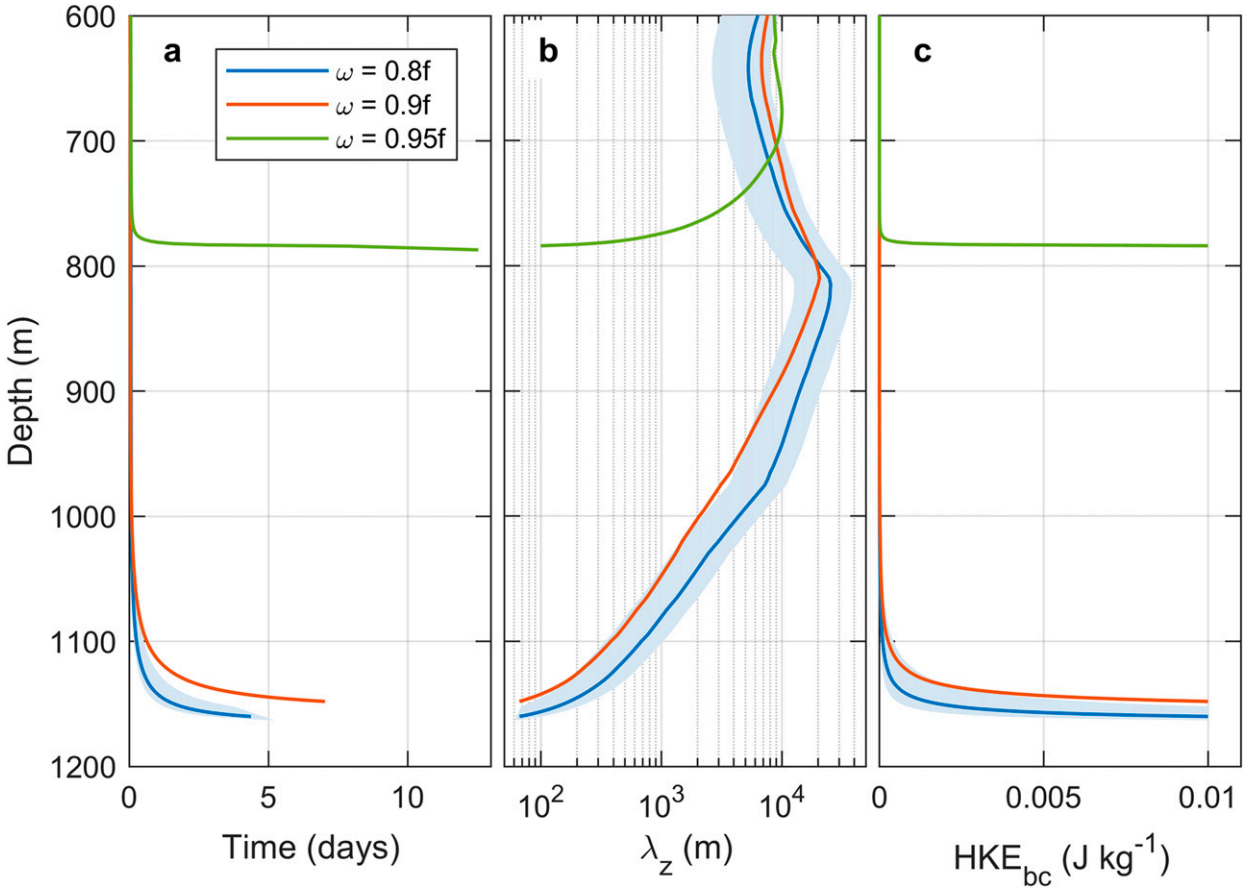

FIG. 13. Vertical profiles of (a) time elapsed, (b) vertical wavelength, and (c) baroclinic horizontal kinetic energy HKE_{bc} for three selected waves released at 50-m depth (see Fig. 9 for the characteristics). Wave vectors are chosen such that their terminal vertical wavelength is between 70 and 100 m and their HKE_{bc} is 10^{-2} J kg^{-1}. An arbitrary horizontal wavelength of 100 km is prescribed. The shading for 0.8*f* shows the sensitivity to horizontal wavelengths of 50–150-km range.

When contrasted to a reference station in the eastern part of the basin, dissipation rates in the LBE are up to two orders of magnitude larger. Turbulence is elevated particularly in the core and at the rim near the velocity maximum, concentrated at two pycnoclines separated by a quiescent pycnostad. The deeper, main pycnocline is located above the base of the LBE. The volume-integrated total energy of the LBE is 9.3×10^{14} J. Our best estimate of volume-integrated dissipation in summer is 2×10^{6} W. The time scale for eddy decay for the total energy is thus approximately 14 years (9 years to drain the horizontal kinetic energy alone). The main pycnocline and the base of the LBE are the main sinks for energy. The turbulent segments below the velocity maximum and near the base of the core are associated with small background gradient Richardson number (equal to or less than unity when computed over 32-m vertical scale). Generation of turbulence by background shear is thus important.

Wavenumber rotary spectra show that the shear variance outside the eddy is small, with no distinct polarization, but the core and rim regions show an amplification of the high-wavenumber clockwise-polarized energy. The spectral properties in the LBE are consistent with downward-propagating near-inertial waves, with vertical wavelength on the order of 100 m and energy levels 3 to 10 times the canonical open-ocean level. The energetic packets with distinct downward energy propagation are detected in individual profiles, which are typically accompanied with increase in dissipation levels. Idealized ray-tracing calculations show that the vertical and lateral changes in stratification, shear, and vorticity allow subinertial waves with low frequencies to be trapped within the LBE. The reflection points and critical layers reflect, focus, and amplify the near-inertial energy, particularly at the rim near the velocity maximum and at base of the core. Amplified energy density near critical layers is suggested as a source for

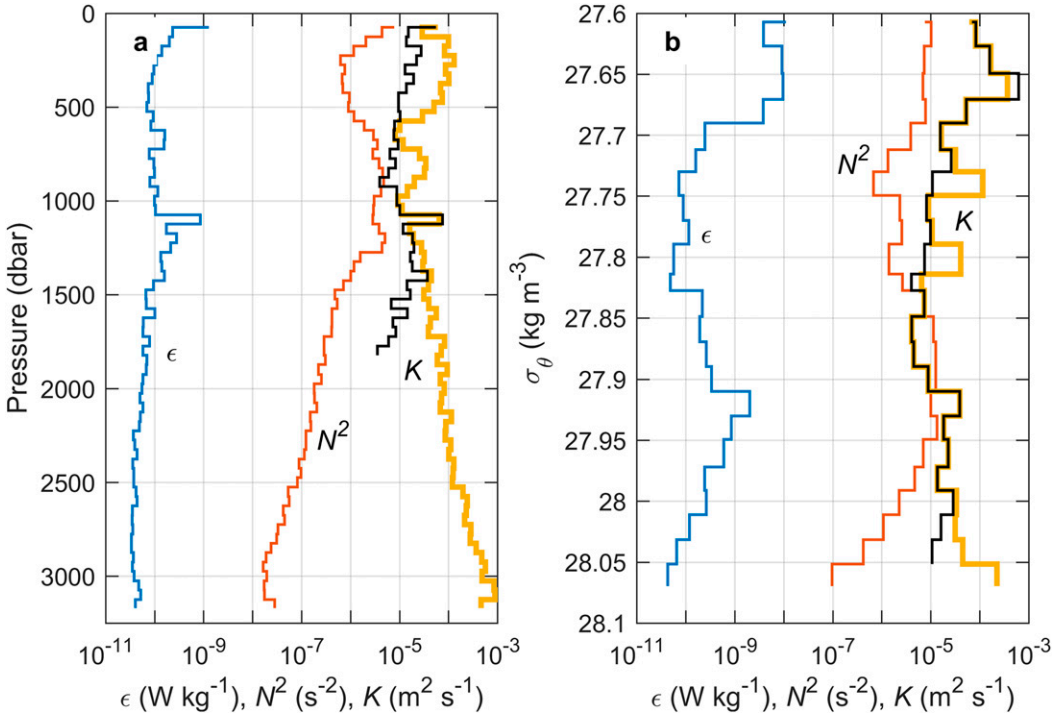

FIG. 14. Survey-averaged profiles of ε, N^2, and diapycnal diffusivity estimated as $K = 0.2\varepsilon/N^2$. Averaging is (a) isobaric using 50-dbar vertical bins and (b) isopycnic using 0.02 σ_θ bins. Average profiles of K are shown using all data segments (yellow) and using averages only over segments (black) with significant stratification (N^2 above the noise level of 10^{-6} s^{-2}).

turbulence. The regions of increased dissipation rates observed in this study are consistent with this interpretation.

The estimated eddy decay time scale due to turbulent dissipation, on the order of one decade, is consistent with a long-lived LBE. However, our summertime observations may not be representative of the importance of frictional losses, as increased dissipation rates may be expected in winter, following cold air outbreaks, storm events, and convection. Winter process studies and year-round measurements, for example, by using gliders, are needed to quantify the energy sources and sinks of the LBE. This feature of about 20-km radius in the Norwegian Sea plays a disproportionately important role in the regional heat, freshwater, and energy distribution and merits further studies.

Acknowledgments. This study received funding from the Research Council of Norway, through the project "Water-mass transformation processes and vortex dynamics in the Lofoten Basin of the Norwegian Sea (ProVoLo)", Project 250784. Henrik Søiland processed the VMADCP data and advised in detecting the LBE core during the cruise. We thank two anonymous reviewers for their constructive comments and Dan Whitt for making his ray-tracing algorithm available.

REFERENCES

Bosse, A., P. Testor, L. Mortier, L. Prieur, V. Taillandier, F. d'Ortenzio, and L. Coppola, 2015: Spreading of Levantine Intermediate Waters by submesoscale coherent vortices in the northwestern Mediterranean Sea as observed with gliders. *J. Geophys. Res. Oceans*, **120**, 1599–1622, https://doi.org/10.1002/2014JC010263.

Bouffard, D., and L. Boegman, 2013: A diapycnal diffusivity model for stratified environmental flows. *Dyn. Atmos. Oceans*, **61–62**, 14–34, https://doi.org/10.1016/j.dynatmoce.2013.02.002.

Cairns, J. L., and G. O. Williams, 1976: Internal wave observations from a midwater float, 2. *J. Geophys. Res.*, **81**, 1943–1950, https://doi.org/10.1029/JC081i012p01943.

Chavanne, C. P., E. Firing, and F. Ascani, 2012: Inertial oscillations in geostrophic flow: Is the inertial frequency shifted by $\zeta/2$ or by ζ? *J. Phys. Oceanogr.*, **42**, 884–888, https://doi.org/10.1175/JPO-D-12-031.1.

Clément, L., and A. M. Thurnherr, 2018: Abyssal upwelling in mid-ocean ridge fracture zones. *Geophys. Res. Lett.*, **45**, 2424–2432, https://doi.org/10.1002/2017GL075872.

Douglas, W., and R. Lueck, 2015: ODAS MATLAB Library technical manual, version 4.0. Rockland Scientific International Inc., https://rocklandscientific.com.

Fer, I., 2016: Cruise report: Cruise HM 2016611 with R.V. Håkon Mosby; 26 May–15 June 2016. University of Bergen Geophysical Institute Rep., 44 pp.

——, R. Skogseth, and F. Geyer, 2010: Internal waves and mixing in the marginal ice zone near the Yermak Plateau.

J. Phys. Oceanogr., **40**, 1613–1630, https://doi.org/10.1175/2010JPO4371.1.

——, A. K. Peterson, and J. E. Ullgren, 2014: Microstructure measurements from an underwater glider in the turbulent Faroe Bank Channel overflow. *J. Atmos. Oceanic Technol.*, **31**, 1128–1150, https://doi.org/10.1175/JTECH-D-13-00221.1.

Ferron, B., F. Kokoszka, H. Mercier, and P. Lherminier, 2014: Dissipation rate estimates from microstructure and finescale internal wave observations along the A25 Greenland–Portugal OVIDE line. *J. Atmos. Oceanic Technol.*, **31**, 2530–2543, https://doi.org/10.1175/JTECH-D-14-00036.1.

Hebert, D., 1988: The available potential energy of an isolated feature. *J. Geophys. Res.*, **93**, 556–564, https://doi.org/10.1029/JC093iC01p00556.

Garrett, C. J., and W. H. Munk, 1975: Space-time scales of internal waves: A progress report. *J. Geophys. Res.*, **80**, 291–297, https://doi.org/10.1029/JC080i003p00291.

McDougall, T. J., and Coauthors, 2010: The international thermodynamic equation of seawater—2010: Calculation and use of thermodynamic properties. Intergovernmental Oceanographic Commission Manuals and Guides 56, 218 pp.

Ivanov, V., and A. A. Korablev, 1995a: Dynamics of an intrapycnocline lens in the Norwegian Sea. *Russ. Meteor. Hydrol.*, **10**, 32–37.

——, and ——, 1995b: Formation and regeneration of the pycnocline lens in the Norwegian Sea. *Russ. Meteor. Hydrol.*, **9**, 62–69.

Joyce, T. M., J. M. Toole, P. Klein, and L. N. Thomas, 2013: A near-inertial mode observed within a Gulf Stream warm-core ring. *J. Geophys. Res. Oceans*, **118**, 1797–1806, https://doi.org/10.1002/jgrc.20141.

Köhl, A., 2007: Generation and stability of a quasi-permanent vortex in the Lofoten Basin. *J. Phys. Oceanogr.*, **37**, 2637–2651, https://doi.org/10.1175/2007JPO3694.1.

Kunze, E., and J. M. Toole, 1997: Tidally driven vorticity, diurnal shear, and turbulence atop Fieberling Seamount. *J. Phys. Oceanogr.*, **27**, 2663–2693, https://doi.org/10.1175/1520-0485(1997)027<2663:TDVDSA>2.0.CO;2.

——, and E. Boss, 1998: A model for vortex-trapped internal waves. *J. Phys. Oceanogr.*, **28**, 2104–2115, https://doi.org/10.1175/1520-0485(1998)028<2104:AMFVTI>2.0.CO;2.

——, R. W. Schmitt, and J. M. Toole, 1995: The energy balance in a warm-core ring's near-inertial critical layer. *J. Phys. Oceanogr.*, **25**, 942–957, https://doi.org/10.1175/1520-0485(1995)025<0942:TEBIAW>2.0.CO;2.

Leaman, K. D., and T. B. Sanford, 1975: Vertical energy propagation of inertial waves: A vector spectral analysis of velocity profiles. *J. Geophys. Res.*, **80**, 1975–1978, https://doi.org/10.1029/JC080i015p01975.

Lueck, R. G., and T. Osborn, 1986: The dissipation of kinetic energy in a warm-core ring. *J. Geophys. Res.*, **91**, 803–818, https://doi.org/10.1029/JC091iC01p00803.

Naveira Garabato, A. C., K. I. C. Oliver, A. J. Watson, and M.-J. Messias, 2004: Turbulent diapycnal mixing in the Nordic seas. *J. Geophys. Res.*, **109**, C12010, https://doi.org/10.1029/2004JC002411.

Nencioli, F., V. S. Kuwahara, T. D. Dickey, Y. M. Rii, and R. R. Bidigare, 2008: Physical dynamics and biological implications of a mesoscale eddy in the lee of Hawai'i: Cyclone Opal observations during E-Flux III. *Deep-Sea Res. II*, **55**, 1252–1274, https://doi.org/10.1016/j.dsr2.2008.02.003.

Orvik, K. A., and P. Niiler, 2002: Major pathways of Atlantic water in the northern North Atlantic and Nordic seas toward Arctic. *Geophys. Res. Lett.*, **29**, 1896, https://doi.org/10.1029/2002GL015002.

Osborn, T. R., 1980: Estimates of the local rate of vertical diffusion from dissipation measurements. *J. Phys. Oceanogr.*, **10**, 83–89, https://doi.org/10.1175/1520-0485(1980)010<0083:EOTLRO>2.0.CO;2.

Polzin, K. L., J. M. Toole, and R. W. Schmitt, 1995: Finescale parameterizations of turbulent dissipation. *J. Phys. Oceanogr.*, **25**, 306–328, https://doi.org/10.1175/1520-0485(1995)025<0306:FPOTD>2.0.CO;2.

——, E. Kunze, J. Hummon, and E. Firing, 2002: The finescale response of lowered ADCP velocity profiles. *J. Atmos. Oceanic Technol.*, **19**, 205–224, https://doi.org/10.1175/1520-0426(2002)019<0205:TFROLA>2.0.CO;2.

Raj, R. P., J. A. Johannessen, T. Eldevik, J. E. Nilsen, and I. Halo, 2016: Quantifying mesoscale eddies in the Lofoten Basin. *J. Geophys. Res. Oceans*, **121**, 4503–4521, https://doi.org/10.1002/2016JC011637.

Richards, C. G., and F. Straneo, 2015: Observations of water mass transformation and eddies in the Lofoten Basin of the Nordic seas. *J. Phys. Oceanogr.*, **45**, 1735–1756, https://doi.org/10.1175/JPO-D-14-0238.1.

Rossby, T., M. D. Prater, and H. Søiland, 2009: Pathways of inflow and dispersion of warm waters in the Nordic seas. *J. Geophys. Res.*, **114**, C04011, https://doi.org/10.1029/2008JC005073.

Sheen, K. L., J. A. Brearley, A. C. Naveira Garabato, D. A. Smeed, L. S. Laurent, M. P. Meredith, A. M. Thurnherr, and S. N. Waterman, 2015: Modification of turbulent dissipation rates by a deep Southern Ocean eddy. *Geophys. Res. Lett.*, **42**, 3450–3457, https://doi.org/10.1002/2015GL063216.

Søiland, H., L. Chafik, and T. Rossby, 2016: On the long-term stability of the Lofoten Basin eddy. *J. Geophys. Res. Oceans*, **121**, 4438–4449, https://doi.org/10.1002/2016JC011726.

Thurnherr, A. M., 2010: A practical assessment of the errors associated with full-depth LADCP profiles obtained using Teledyne RDI Workhorse acoustic Doppler current profilers. *J. Atmos. Oceanic Technol.*, **27**, 1215–1227, https://doi.org/10.1175/2010JTECHO708.1.

Visbeck, M., 2002: Deep velocity profiling using lowered acoustic Doppler current profilers: Bottom track and inverse solutions. *J. Atmos. Oceanic Technol.*, **19**, 794–807, https://doi.org/10.1175/1520-0426(2002)019<0794:DVPULA>2.0.CO;2.

Volkov, D. L., A. A. Kubryakov, and R. Lumpkin, 2015: Formation and variability of the Lofoten Basin vortex in a high-resolution ocean model. *Deep-Sea Res. I*, **105**, 142–157, https://doi.org/10.1016/j.dsr.2015.09.001.

Whitt, D. B., and L. N. Thomas, 2013: Near-inertial waves in strongly baroclinic currents. *J. Phys. Oceanogr.*, **43**, 706–725, https://doi.org/10.1175/JPO-D-12-0132.1.

——, and ——, 2015: Resonant generation and energetics of wind-forced near-inertial motions in a geostrophic flow. *J. Phys. Oceanogr.*, **45**, 181–208, https://doi.org/10.1175/JPO-D-14-0168.1.

——, ——, J. M. Klymak, C. M. Lee, and E. A. D'Asaro, 2018: Interaction of superinertial waves with submesoscale cyclonic filaments in the north wall of the Gulf Stream. *J. Phys. Oceanogr.*, **48**, 81–99, https://doi.org/10.1175/JPO-D-17-0079.1.

Yu, L.-S., A. Bosse, I. Fer, K. A. Orvik, E. M. Bruvik, I. Hessevik, and K. Kvalsund, 2017: The Lofoten Basin eddy: Three years of evolution as observed by Seagliders. *J. Geophys. Res. Oceans*, **122**, 6814–6834, https://doi.org/10.1002/2017JC012982.